1 **Methods**

2 S1. Empirical Mode Decomposition (EMD)

3   Empirical Mode Decomposition (EMD) is a data-driven technique used to decompose a signal

4 into a set of intrinsic mode functions (IMFs) and a residual trend (Huang et al., 1998). It is

5 particularly suitable for analyzing nonlinear and non-stationary time series data. Many studies have

6 shown that the residuals of EMD can reflect the deterministic trend of non-stationary sequences (Lee

7 and Ouarda, 2010; Qian, 2016; Wu et al., 2023). In this study, the EMD is applied to quantify the

8 deterministic trends in the recurrence hazards of compound extreme events. The formula is as

9 follows:

10
$$x(t) = \sum_{i=1}^{n} IMF_i(t) + r_n(t)$$

11 $x(t)$ is the original signal. $IMF_i(t)$ represents the i-th intrinsic mode function, which is the result

12 of the decomposition. $r_n(t)$ is the residual (a trend or constant component left after the

13 decomposition). Typically, it is a constant or a slowly varying trend.

14 **Results**

15 S1 Assessing the regional applicability of downscaled CMIP6bc based on historical data

16   Although the quality of CMIP6bc has been widely validated across China, a regional

17 applicability assessment remains necessary. Figure S1 illustrates the spatiotemporal patterns of

18 precipitation and temperature simulated by the WRF model using different driving datasets.

19 Compared to observations, both the downscaled ERA5 and CMIP6bc demonstrated satisfactory

20 performance in reproducing the spatio-temporal distribution characteristics of precipitation and

21 temperature across the MRB (Figures S1 a–f). Specifically, the ERA5-based simulations outperform

22 CMIP6bc, particularly for precipitation (CC = 0.88, PBIAS = 3.79%) compared to temperature (CC

23 = 0.80; PBIAS = 4.03%). However, the models demonstrate consistent underestimations in the

24 downstream areas and overestimations in the northwestern Wuyi Mountain region. These systematic

25 biases are likely attributable to orographic effects, with the WRF model consistently underestimating

26 precipitation in plain areas while overestimating it in high-elevation regions (Wang et al., 2020; Min

27 et al., 2021). As shown in Figures S1 (g, h), the results from both driving datasets capture the

28 observed temporal variations, with temperature simulations showing better agreement than

29 precipitation. The Taylor diagrams in Figures S1 (i–l) reveal that the WRF model's performance is

30 comparatively weaker in the downstream sub-basin of the MRB than the other three sub-basins. In

31 summary, although CMIP6bc underperforms ERA5 due to resolution limitations, it still exhibits

32 reasonable spatio-temporal consistency with the observations. We conclude that such discrepancies

33 remain within an acceptable range for subsequent research.

34   **Table**

35   Table S1 Distribution functions in this study.

| Distribution function	Abbreviation	Number of parameters
Gamma	GA	2
Gumbel	GU	2
Inverse Gamma	IGAMMA	2
Inverse Gaussian	IG	2
Logistic	LO	2
Log-Normal	LOGNO	2
Reverse Gumbel	RG	2
Weibull	WEI3	2
Normal	NO	2
Exponential gen. beta 2	EGB2	4
Johnson's SU repar.	JSU	4
Johnson's original SU	JSUo	4
Generalised t	GT	4
SU	SU	4
NET	NET	4
Sinh-arcsinh	SHASH	4
Sinh-arcsinh original	SHASHo	4
Sinh-arcsinh original 2	SHASHo2	4

36
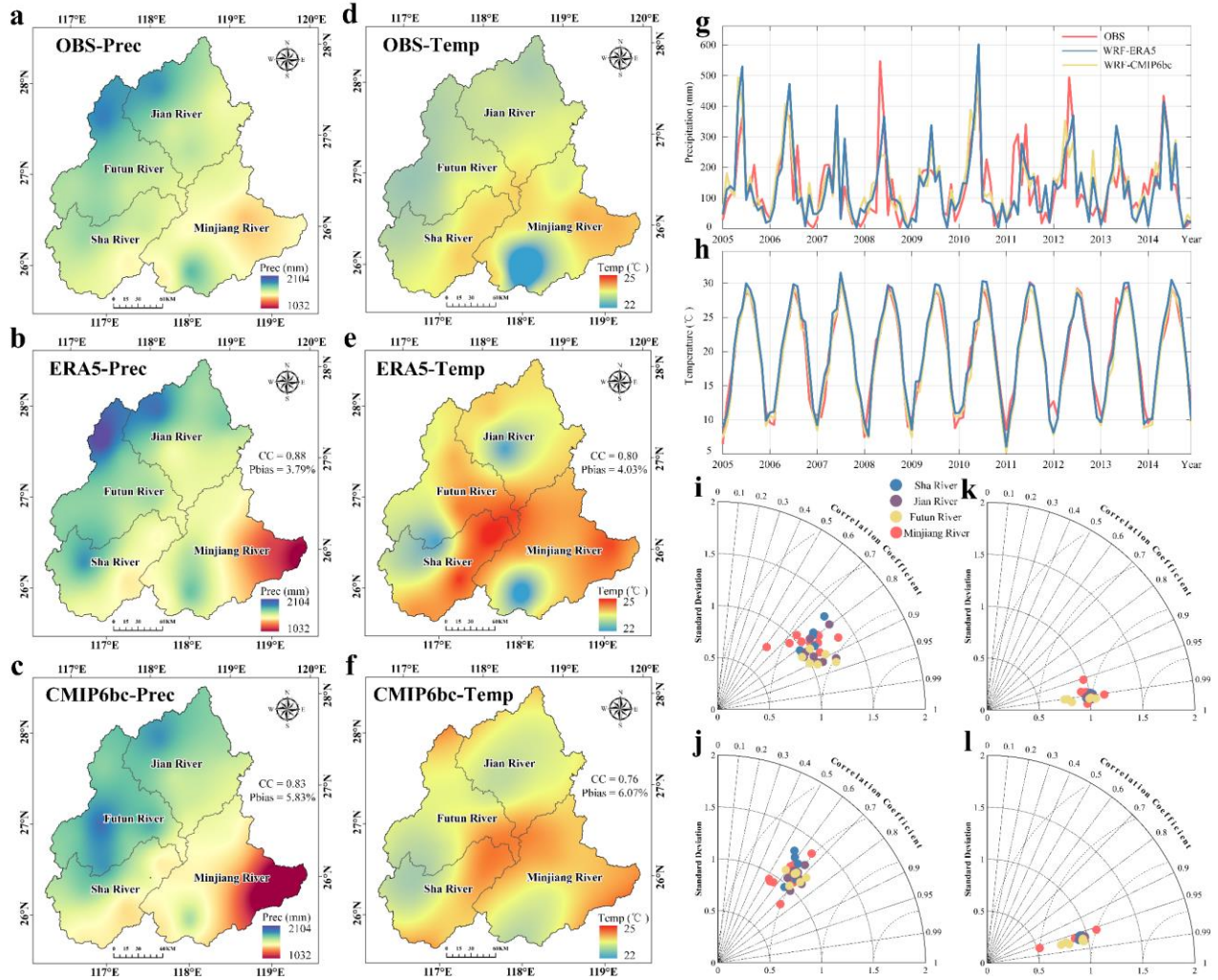
Figure

Figure S1. Evaluation of WRF-simulated precipitation and temperature over the MRB (2005- 2014). spatial patterns of precipitation (a–c), temperature (d–f). Temporal evolution of precipitation (g) and temperature (h). Panels (i–l) present sub-basin comparisons of precipitation and temperature from ERA5 (i, k) and CMIP6bc (j, l).
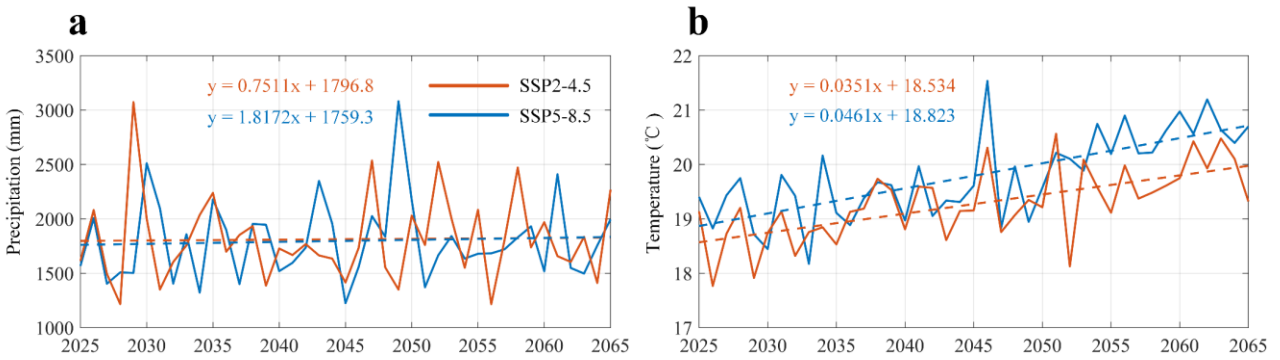

Figure S2 Variation of in annual precipitation (a) and temperature (b) in MRB from 2025 to 2065.
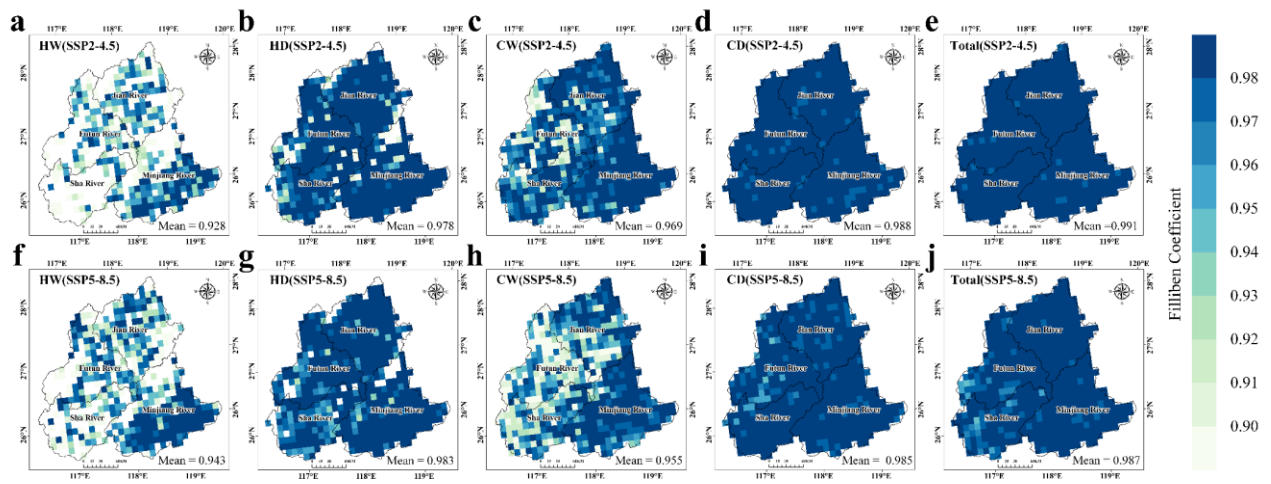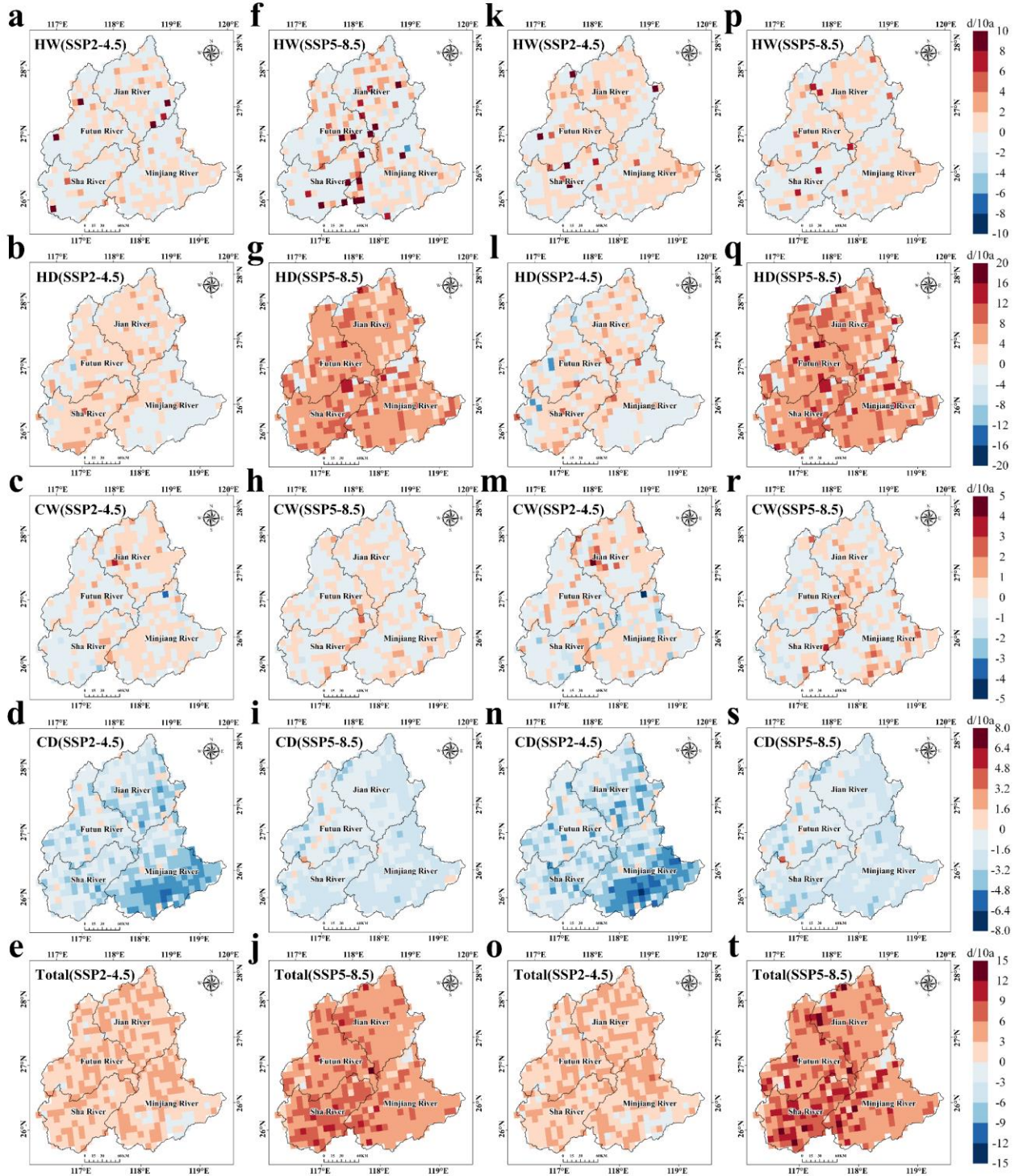
45

46   Figure S3 Maps of the Filliben Coefficient for CCEs.

20-year return periods   50-year return periods

47

48   Figure S4 As in Figure 7 but for 20- and 50- return periods.

49 **References**

50 Huang, N.E., Shen, Z., Long, S.R., Wu, M.C., Shih, H.H., Zheng, Q., Yen, N.-C., Tung, C.C., Liu,

51 H.H., 1998. The empirical mode decomposition and the Hilbert spectrum for nonlinear and non-

52 stationary time series analysis. Proc. R. Soc. Lond. A. 454, 903–995.

53 https://doi.org/10.1098/rspa.1998.0193

54 Lee, T., Ouarda, T.B.M.J., 2010. Long-term prediction of precipitation and hydrologic extremes with

55 nonstationary oscillation processes. J. Geophys. Res. 115, 2009JD012801.

56 https://doi.org/10.1029/2009JD012801

57 Min, Y., Huang, W., Ma, M., Zhang, Y., 2021. Simulations in the topography effects of Tianshan

58 Mountains on an extreme precipitation event in the Ili River Valley, China. Atmosphere 12, 750.

59 https://doi.org/10.3390/atmos12060750

60 Qian, C., 2016. On trend estimation and significance testing for non-Gaussian and serially dependent

61 data: quantifying the urbanization effect on trends in hot extremes in the megacity of Shanghai. Clim.

62 Dyn. 47, 329–344. https://doi.org/10.1007/s00382-015-2838-0

63 Wang, Y., Yang, K., Zhou, X., Chen, D., Lu, H., Ouyang, L., Chen, Y., Lazhu, Wang, B., 2020.

64 Synergy of orographic drag parameterization and high resolution greatly reduces biases of WRF-

65 simulated precipitation in central Himalaya. Clim. Dyn. 54, 1729–1740.

66 https://doi.org/10.1007/s00382-019-05080-w

67 Wu, J., Wang, Z., Dong, J., Cui, X., Tao, S., Chen, X., 2023. Robust Runoff Prediction With

68 Explainable Artificial Intelligence and Meteorological Variables From Deep Learning Ensemble

69 Model. Water Resour. Res. 59, e2023WR035676. https://doi.org/10.1029/2023WR035676